RSC Advances

PAPER

View Article Online
View Journal | View Issue

Cite this: *RSC Adv.*, 2021, **11**, 37700

Efficient Na^+-storage in a $Li_4Ti_5O_{12}$ anode to expand the voltage-window for full SIBs of high energy density†

Chao Li,*[a] Binhui Luo,[a] Youman Zhao,[b] Yongsheng Chen,[a] Hua Yang,*[c] Jingang Song,[a] Lili Zhao[a] and Xiaobo Fu[a]

The stable storage of sodium ions always presents some difficulties for sodium-based dual-ion batteries (S-DIBs), such as the irreversibility of guest-storage and kinetic hindrance in the anode. Based on the low strain volume and stable phase structure, herein, lithium titanate (LTO, $Li_4Ti_5O_{12}$) was developed to store sodium ions between the working potential (~0.8 V), which expands the lower plateau over than that of lithium ion storage (~1.55 V) to obtain a high energy density of full batteries. The spinel lithium titanate shows negligible volume change and extremely stable structure under Na^+-storage, which completely overcomes the shortage problems of the Na^+-host. Additionally, by the detection of the transfer state of anions and cations in dual-ion batteries, the diffusion coefficient of the sodium ion in the LTO electrode is higher than that of the cathode, which shows that the transport process of sodium ions can meet the kinetic demands of full batteries. Such S-DIBs exhibit a large working voltage of 2.0–4.6 V and stable electrochemical performance over 1280 cycles, which is superior to conventional sodium-based systems, and further exhibit many advantages such as high energy density, environmental friendliness, and low cost.

Received 20th August 2021
Accepted 24th September 2021

DOI: 10.1039/d1ra06313h

rsc.li/rsc-advances

1 Introduction

Currently, some sodium-storage chemical systems have attracted tremendous attention as next-generation energy storage materials, such as sodium ion batteries (SIBs), sodium-based dual-ion batteries (S-DIBs) and sodium metal batteries (SMBs), which is attributed to the rich availability of the required natural resources and low costs compared to conventional lithium-ion batteries (LIBs). However, the storage host material of sodium ions has always affected the development of sodium-based batteries, owing to the larger diameter of sodium ions leading to slow de/intercalation kinetics and an unstable ion-storage process, whether in cathode or anode materials.[1–4] For the cathodes of sodium storage, dual-ion batteries (DIBs) can ideally avoid this key problem, which is attributed to the special storage mechanism of anion intercalation in the cathode. In DIBs, the layered materials, such as graphite or other layered materials, are usually the anion storage host. Thus, S-DIBs can solve a part of the important problems faced by sodium-ion storage systems and help them exhibit some indispensable advantages.

Therefore, the key focus of S-DIBs is on anode materials, where there is a stable host structure for storing sodium ions and for realizing fast ion transfer kinetic channels. In this case, many anode materials are prepared to form some practical full S-DIBs, such as metal Na plate,[5,6] Sn metal,[7] soft carbon,[8] and hard carbon,[9] and demonstrate some application potential. However, alloyed materials also retain some problems owing to their highly irreversible reactions, oxygen activity, and low safety, especially metal Na.[10] Additionally, for most anode materials in LIBs, the low kinetic diffusion of sodium ions also leads to poor cycling and power capability.

At the same time, many researchers have proposed a variety of cathode materials for storing sodium ions,[1] such as phosphates, pyrophosphates, fluorosulfates, oxychlorides, and organic compounds, and exhibiting stable electrochemical capability. However, owing to the higher standard potential (~2.71 V *vs.* SHE as compared to the 3.02 V *vs.* SHE for lithium) of sodium ions,[11,12] the decreasing voltage window limits the enhancement of the energy density for full batteries. In addition, repetitive phase evolution into the host structure is inevitable during sodium ion intercalation because of the large size of Na^+ (1.02 Å *vs.* 0.76 Å, ~Li^+). Thus, it is difficult for its electrochemical performance to achieve the level of similar industrialized LIBs.[13] In order to increase the voltage and cyclic

[a]College of Chemical Engineering and Energy Technology, Dongguan University of Technology, Dongguan 523808, China. E-mail: lichao@dgut.edu.cn; dglichao520@126.com; Tel: +86-136-50451058

[b]Chuangming Battery Technology Co., Ltd. of Dongguan City, Dongguan 523808, China

[c]Dongguan Neutron Science Center, No. 1 Zhongziyuan Road, Dalang, Dongguan 523803, China

† Electronic supplementary information (ESI) available. See DOI: 10.1039/d1ra06313h

stability of SIBs, the S-DIBs based on the graphite cathode is better than the traditional SIBs, mainly due to the high voltage range (more than 4 V) and the improved dynamic performance based on anion storage for graphite. For the application of S-DIBs, the key focus has been on matching anode materials for storing sodium ions. Thus, it is necessary to further search for more suitable anode materials to intercalate the sodium ions.

As is well known, lithium titanate (LTO, $Li_4Ti_5O_{12}$) is one of the most promising anode materials in LIBs due to its unique characteristics, such as "zero-strain" in the lattice on the charge/discharge process and the theoretical capacity of 177 mA h g^{-1}, resulting in excellent long-life over ten thousand cycles simultaneously.[14,15] Recently, researchers have found that LTO can also store Na^+ ions by intercalation and deintercalation, same as that of the type of Li^+-storage. Sun *et al.* reported that the LTO of Na^+-storage can display a theoretical capacity of 175 mA h g^{-1} in SIBs.[16,17] DFT calculations can even predict three-phase separation mechanism for the intercalation of Na^+, and the coexistence of $Li_7Ti_5O_{12}$ and $Na_6LiTi_5O_{12}$.

$$2Li_4Ti_5O_{12} + 6Na^+ + 6e^- \rightarrow Li_7Ti_5O_{12} + Na_6LiTi_5O_{12}$$

After employing the sodium ion as the guest, the LTO shows extremely wide application due to its wider voltage range and higher energy density of the energy storage device.

In theory, we envision that the possibility of LTO is used as a host material to store sodium ions in DIBs. Nevertheless, the intercalated behaviors and its electrochemical properties of sodium ions still remain unclear in full SIBs. In particular, the difference in the structure and the electrochemical differences should be studied after the intercalation of Na^+ and Li^+ ions.[18] In this study, the LTO material is employed as the Na^+-storage anode for S-DIBs. Through the comparison of electrochemical performance and structural change for the intercalation of both the ions, the LTO anode presents excellent long cycling, especially the obvious increase in the voltage window and energy density in full batteries, as shown in Fig. 1. After analyzing the kinetics of Na^+-transport in the phase structure, the high-performance of S-DIBs can be enabled by the synchronous (de)intercalation capability of Na^+ in LTO.

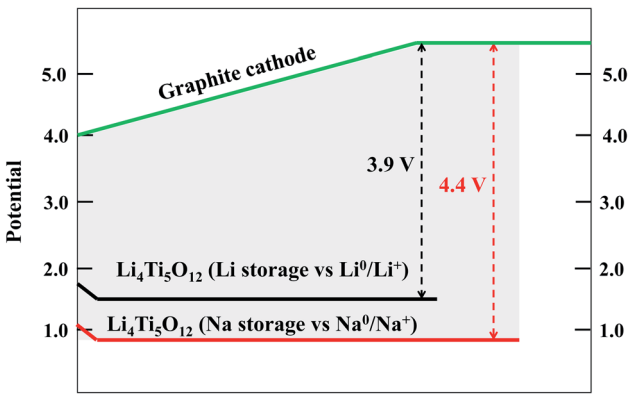

Fig. 1 Voltage profiles of the $Li_4Ti_5O_{12}$ anode and the graphite cathode in the lithium-based and sodium-based chemical system of dual-ion batteries.

2 Experimental

2.1 Materials and electrodes

For the $Li_4Ti_5O_{12}$ material, the nanomaterial is used as the target material from the Shenzhen BTR new material. The active anode, carboxymethyl cellulose sodium (CMC, Aladdin M.W. 90 000), styrene butadiene rubber (SBR, Kosyn LATEX KL341, South Korea), and a conductive agent (Super-P, Timical) were mixed in the weight ratio of 7 : 0.5 : 1 : 1.5 in DI water. The resultant slurry was coated onto a copper foil by an automatic coating machine. Also, the loading mass was 32.5 g m^{-2} for the $Li_4Ti_5O_{12}$ electrode. The prepared electrode was dried at 110 °C under vacuum for 6 h to evaporate the water.

Next, 1 M $LiPF_6$ or $NaPF_6$ was added into the PC/EMC (3 : 7 wt% ratio) solvent, which was used as the electrolyte. They were obtained from JinGuang High-tech (99.99% purity) Co. Ltd.

2.2 Electrochemical characterization

For the electrodes in the half-cells and full-batteries, the thickness of the electrode was strictly controlled by the thickness control mold. The proportion of the loading mass for the cathode and anode was taken according to the design of the stoichiometry for the purpose of the experiment. These electrodes were dried at 120 °C under vacuum for 6 h. The half-cells and full-batteries (CR2032) were assembled in a glove box filled with dry Ar atmosphere. The electrolyte in the PC : EMC (3 : 7) solvent was used. The lithium salts had the concentrations of 1 M $LiPF_6$ or $NaPF_6$. Electrochemical characterization was conducted using the galvanostatic charge–discharge tests (LAND 2001 CT battery tester). Cyclic voltammetry (CV) curves were collected using the electrochemical workstation with the scanning rate of 0.1, 0.2, 0.4, and 0.8 mV s^{-1}. SEM observations were carried out using an XL-30 microscope (Quanta FEG, FEI, PHILIPS). The residual pressure in the Raman and XRD analysis chamber was 9.3 × 10^{-7} Pa. To avoid any contamination from oxygen and water, the cycled electrodes were transferred from the Ar-filled glove box to the chamber using a special air-proof device. XRD studies were carried out using a D8 Advance diffraction system (Bruker, Germany). Raman studies were carried out using the measuring platform (HORIBA XploRA PLUS). In addition, the raw spectra was curve-fitted by nonlinear least squares fittings with a Gauss-Lorentz ratio (80 : 20) using the XPSPEAK41 software. Electrochemical impedance spectroscopy (EIS) was employed using the electrochemical workstation of GAMRY Interface 1000, and the scanning frequency was set in the range of 0.1–100 000 Hz.

3 Results and discussion

The prepared-LTO shows nanometer particles and standard crystal structure, as obtained from SEM and XRD in Fig. 2, S1 and S2.† Fig. 2a and b compare the charge–discharge curves

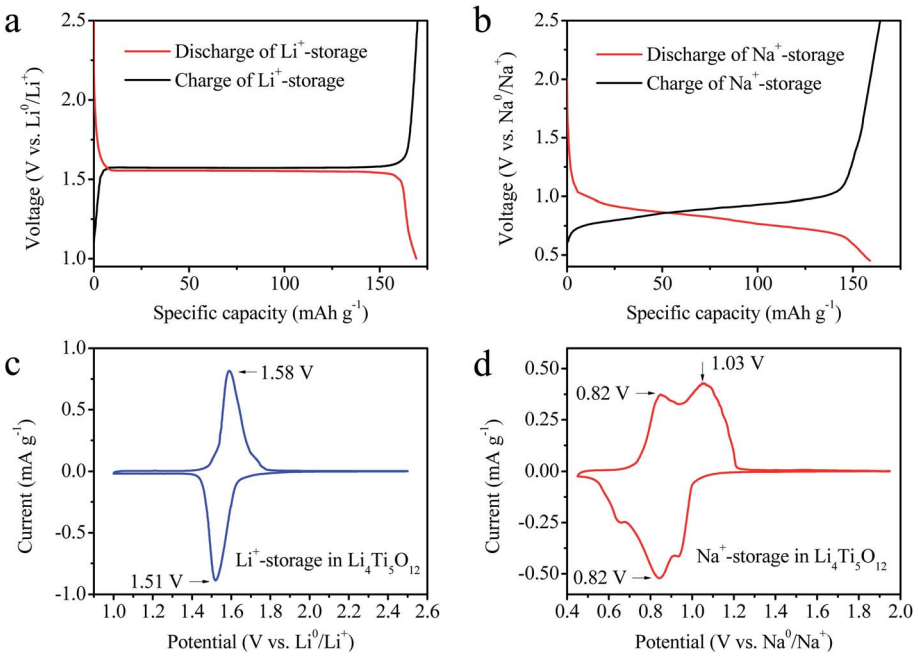

Fig. 2 The charge–discharge curves of the (a) lithium-based and (b) sodium-based $Li_4Ti_5O_{12}$ half-cell; the cyclic voltammetry curves of the (c) lithium-based and (d) sodium-based $Li_4Ti_5O_{12}$ half-cell.

during the first-cycle for Li^+-storage and Na^+-storage in the nanometer LTO electrode. It is known that the potential plateaus at ~1.55 V were exhibited for Li^+-storage, mainly due to the two-phase transition between the spinel structure (space group $Fd\bar{3}m$) and the rock-salt phase (space group $Fm\bar{3}m$).[2,19] Instead, the LTO electrode for Na^+-storage shows a potential drop from open circuit voltage (OCV) to 1 V and a gradual potential decrease from ~1 to ~0.4 V; thus, the potential plateau of the drop line is different for the curves of Li^+-storage. The electrode for Na^+-storage demonstrates a specific capacity of 159.2 mA h g^{-1}, which is slightly lower than the capacity of Li^+-storage (~168 mA h g^{-1}). Also, the reversible process also shows similar characteristics for charge and discharge. At the same time, the CV curves of Li^+-storage and Na^+-storage are measured in the potential window of 0.4/2.0 V with a scan rate 0.1 mV s^{-1}, as shown in Fig. 2c and d. The sample of Li^+-storage exhibits common properties between a cathodic peak at 1.51 V and anodic peak at 1.58 V, which is the same as the (dis)charge curves. Unlike that of Li^+-storage, the sample of Na^+-storage presents a pair of broad current peaks, and appears at 0.85 V of the cathodic peak and 1.1 V of the anodic peak. The shape of the above peaks verifies the three-phase separation process during the intercalation of Na^+ ions from the previous studies.[20,21] Some small peaks next to the main peak can also testify the phase transition. In addition, the peak-to-peak splitting for the cathodizing and anodizing of the Na^+-storage is obviously larger compared to that of the Li^+-storage. This splitting is attributed to the increasing kinetic impedance for Na^+ in the nano-crystalline phase, which is consistent with the previous reports.[16,22] Chronopotentiometric measurement confirms that the diffusion and intercalation of Na^+ into the nanomaterials maybe present some problems.

In order to compare the kinetic behavior of both kinds of ions in the LTO phase, the galvanostatic intermittent titration technique (GITT) is applied during the charge and discharge process.[23] Fig. 3a and b describe the curves of GITT under discharge–charge after pre-cycling. It can be seen from the curves that the voltage trends are different but the change trends are basically corresponding to the charge–discharge curves in Fig. 2a and b under the near-equilibrium state. The diffusion coefficients of the ions are calculated under different state of charge (SOC) from the GITT curves, combined with Fick's second law.[24,25]

$$D = \frac{4}{\pi}\left(\frac{m_B V_M}{M_B S}\right)^2 \left(\Delta E_S \Big/ \tau\left(\frac{dE_\tau}{d\sqrt{\tau}}\right)\right)^2 \quad \left(t \ll \frac{L^2}{D}\right)$$

here, m_B, M_B, V_M, and S are defined as the molar weight, LTO mass, molecular volume, and geometric area of the materials, respectively. Also, τ, ΔEs, and $E\tau$ are the duration time of the current pulse, voltage change at the steady state, and transient voltage during the titration process.[26] In the GITT experiment, the voltage window of the LTO anode is selected at 1–2.5 V for Li^+-storage and 0.25–2.25 V for Na^+-storage by a series of intermittent current (100 mA g^{-1}) for 30 min and then kept still at the open circuit for 10 h. The calculated data of the diffusion coefficient (D_s) are demonstrated in Fig. 3c and d. More importantly, the D_s of Na^+ in the LTO (~10^{-12} to 10^{-15} cm^2 s^{-1}) is slightly lower than that of Li^+ (~10^{-12} to 10^{-16} cm^2 s^{-1}), and the value depends on the state of charge (SOC). For Na^+-storage, the D_s is obviously low under the state of poor-Na^+ and rich-Na^+, in other words, the materials as the phase of $Li_4Ti_5O_{12}$ and $LiNa_3Ti_5O_{12}$. At the same time, it also reflects that the diffusion impedance of Na^+-storage is higher than that of Li^+-storage,

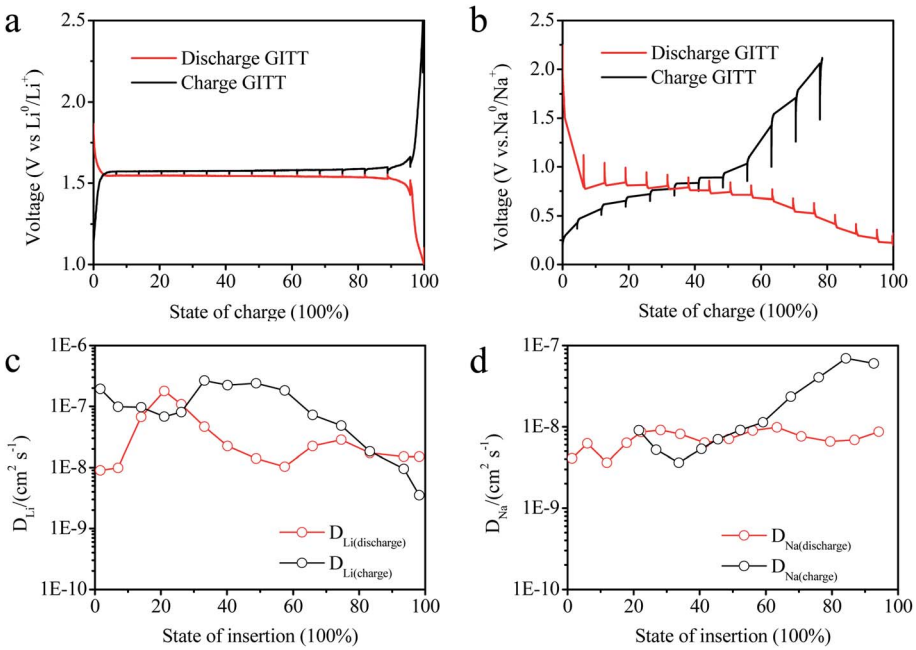

Fig. 3 The GITT curves and ion diffusion coefficient of the (a), (c) lithium-based and (b), (d) sodium-based half-cell.

which leads to the larger splitting voltage and low specific capacity.

Fig. 4a displays the electrochemical cycling curves for Na^+ in the half-cell (LTO|Na) under the rate of 0.5C. In the first cycles, the battery shows the capacity of 166.98 mA h g^{-1} for Na^+-insertion and capacity of 163.53 mA h g^{-1} for Na^+-extraction, which approached the theoretical capacity of LTO. It depicts the stable phase structure used to store Na^+. In the following cycles, the specific capacity of LTO remains above 150 mA h g^{-1} in the first 500 cycles, as shown in Fig. 4b. At the same time, the voltage plateau shows obvious changes for the decrease in the discharge and increase in the charge process. This result can be considered due to the increase in the kinetics polarization and the mass transfer resistance of Na^+ in the LTO phase. Owing to the larger radius of Na^+, the diffusion problem of the interface of the electrode and the electrolyte is still the most possible reason, in comparison to the transmission kinetics in the solid material.

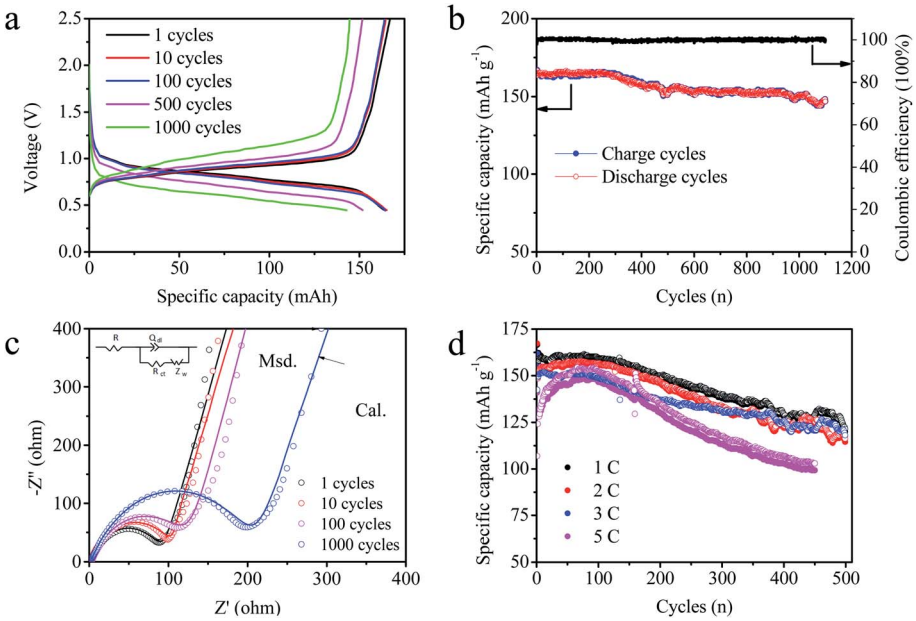

Fig. 4 (a) Charge–discharge curves and (b) life cycling of the $Li_4Ti_5O_{12}$ half-cell, (c) the EIS curves and (d) rate performance.

Electrochemical impedance spectroscopy (EIS) was employed to study the impedance after the (de)intercalation of Na^+ under different cycles (1, 10, 100, and 1000 cycles), as shown in Fig. 4c. The curves exhibit a semicircle at high-middle frequency and a diagonal line at low frequency. Through the simulation of the equivalent circuit (the inset of Fig. 4c), the fitting curves are highly consistent with the real impedance spectrum. After analysis, the part of the semicircle is considered to be the charge transfer resistance (R_{ct}) at the interface related to the alloy of poor-sodium for LTO particles.[27,28] It can be seen that the R_{ct} of the electrode slightly increased from 95.6 Ohm to 100.2 Ohm at 10 cycles but increased to 122.2 Ohm at 100 cycles and further reached 205 Ohm after 1000 cycles, which indicated that the resistance gradually increased from the diffusion capability at the solid–liquid interface.

The rate properties during high current density can reflect the capability of diffusion and intercalation for Na^+ in LTO materials. Fig. 4d presents the cycling curves at the rate of 1C to 5C. In the first cycle, the cell respectively provides the capacities of 164.8, 161.3, 157.2, and 104.3 mA h g^{-1} at four kinds of rates, which decreases according to the increase in the rates. It indicates that Na^+ can quickly transport in nanometer materials under the intercalation reaction process of LTO. For continuous cycling, it can be seen that the performance is relatively stable at 1–3 C, and is slightly worse at 5C but the capacity unexpectedly gradually restored after the first 50 cycles. After 500 cycles, respectively, the capacities were decreased to 120.0, 116.5, 112.0, and 99.3 mA h g^{-1}, and the attenuation rates were 72.8%, 72.1%, 71.2%, and 66.4% (calculated based on the highest specific capacity at the initial 5C rate). Despite such a relatively large capacity drop at the rate of 5C, its capacity remains at a high level in rate compared to the graphite cathode for DIBs.

Very recently, the capability of fast transport for Li^+ in the two-phase reaction was revealed, which are attributed to the kinetics pathway along a two-phase boundary in the presence of metastable intermediates.[29] For the behavior of Na^+ in LTO, we also estimated that Na^+ also reaches intercalation in a similar manner of transport. However, owing to the larger radius of Na^+ (~101 Å) than that of Li^+ (~60 Å), the structural changes may present some differences from Li^+ after the intercalation of Na^+ into the LTO phase.[30] Fig. 5a shows the comparison of the Raman spectra of the LTO phase before and after the intercalation of Li^+ and Na^+ ions. The Raman curve of the fresh electrode (black line) exhibits three main characteristic peaks at 234 cm^{-1}, 424 cm^{-1}, and 674 cm^{-1}, which are assigned to the transport energy of F1g, Eg, and A1g, respectively.[31] For the LTO of the Li^+-storage (red line), the curves show obvious differences from the original characteristic peaks (~fresh electrode), which reflects the weakening of F 1g and red-shifting to a lower wavenumber of Eg and A1g, such as Eg (from 424 cm^{-1} to 410 cm^{-1}) and A1g (from 674 cm^{-1} to 622 cm^{-1}). At the same time, an additional peak at the position of 167 cm^{-1} is attributed to orthorhombic titanate, $Li_{0.5}TiO_2$ (space group *Imma*),[32] which is mainly due to the structure formed by the Li-intercalated tetragonal anatase TiO_2 (space group $I4_1/amd$) at the level of full Li-intercalation ($x \approx 0.5$).[33] However, the Raman spectrum of Na^+-storage (blue line) shows some clear changes occurring within the above regions. The corresponding intensity at 167 cm^{-1} became sharper, which should be due to the intercalation of Na^+, inducing the rearrangement of Li atoms in the original LTO phase into the orthorhombic titanate

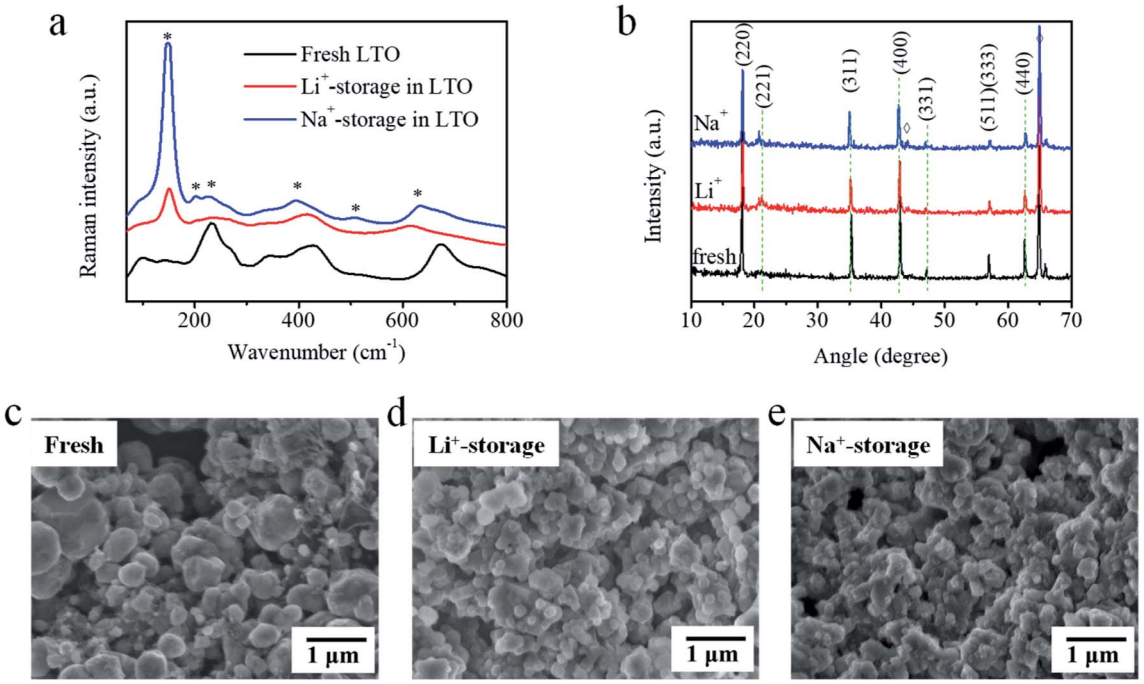

Fig. 5 Comparison of (a) Raman, (b) XRD curves, and (c)–(e) SEM images of $Li_4Ti_5O_{12}$ electrodes before and after the intercalation of lithium ions and sodium ions.

($\sim Li_{0.5}TiO_2$).[20] In addition, a subtle peak appeared at 180 cm^{-1} to the right of 167 cm^{-1}, and it may also be related to the formation of tetragonal anatase, TiO_2.[33] Also, there is still a weak characteristic peak ($\sim$F1g) at the original position of 229 cm^{-1}.[34] At the same time, for the red-shifted Eg and A1g peaks, the region of Eg is shifted to lower wavenumber (red shift), which appeared at 390 cm^{-1}. The Eg peak represents the tensile vibration mode of Li–O in tetrahedra LiO_4; the transport energy of Li–O shows weakening after the intercalation of Na^+ replaces Li^+ in phase.[32] In addition, the A1g peak exhibits stronger intensity without the shifting of position, which indicates the tensile motion mode of Ti–O in octahedra TiO_6. In addition, a subtle but clear peak appeared at the position of 526 cm^{-1}, which is also attributed to the new substance formed by Na^+ and TiO_2. Therefore, Raman spectroscopy confirms that the impact on LTO is stronger for Na^+-storage compared to Li^+-storage owing to the larger radius.

At the same time, X-ray diffraction was conducted to further compare the structural differences in the process of Li^+-storage and Na^+-storage, as illustrated in Fig. 5b. The patterns of fresh-LTO show main peaks appearing at 18.4°, 35.2°, 42.7°, and 62.9°, which are attributed to the peaks of (220), (311), (400), and (440), respectively.[35,36] For the rich-Li^+ and Na^+ electrodes, the characteristic peak is almost the same as that of the fresh electrode. Nonetheless, subtle but clear changes occurred within the side region of the peaks. Interestingly, the diffraction peaks of (221) and (311) at 20.8° and 41.9° for Na^+-storage are shifted on the basis of Li^+-storage.[16] Also, the intensity of the peaks of (331) and (440) at 52.1° and 62.9° becomes weaker.[35,36] As we know that owing to the LTO serving as a "zero strain" anode, the characteristic peaks remain relatively stable but some weak changes still exist, which indicates that the intercalation of Na^+ also bears some influences from the LTO phase.[22] Moreover, Fig. 5c–e displays the morphology of the LTO electrode before and after ion-storage. Combined with the XRD pattern, it can be seen from the SEM results that the shape and distribution of the LTO electrode show no obvious changes after the intercalation of Na^+. Also, the structural characteristics indicate that this material can achieve the stable intercalation–deintercalation of Na^+. Thus, the above results show that the Na^+-storage of LTO materials can increase the voltage window and solve the scarcity of the host for Na^+ guest, although the diffusion properties of Na^+ have slight insufficiency compared to Li^+ storage.[37]

In DIBs, the anions and cations from the electrolyte can be simultaneously intercalated into the anode and cathode electrodes; therefore, the properties of diffusion in both the electrodes for anions and cations play the same important role. To improve the electrochemical performance of DIBs, it is necessary to analyze the diffusion kinetics of the ions in both the materials. Fig. 6a shows that the GITT curves of the layered graphite cathode during charging and discharging (anionic intercalation and de intercalation) process is measured, and that the voltage is the range of 3.5–5 V. According to Fick's second law, the anion diffusion coefficients ($D_{PF_6^-}$) with different insertion ratios are calculated, as shown in Fig. 6b. At the same time, the diffusion coefficient of sodium ions (D_{Na^+}) in the LTO is also compared in the figure. It can be seen from these curves that D_{Na^+} is concentrated in the range of 10^{-8} to 10^{-9} cm^2 s^{-1}, and the maximum value can reach 10^{-7} cm^2 s^{-1} when sodium is fully sodiated. Instead, the $D_{PF_6^-}$ for intercalation and deintercalation is distributed over a wider range with different intercalation states, which are 10^{-11} to 10^{-9} cm^2 s^{-1}, and

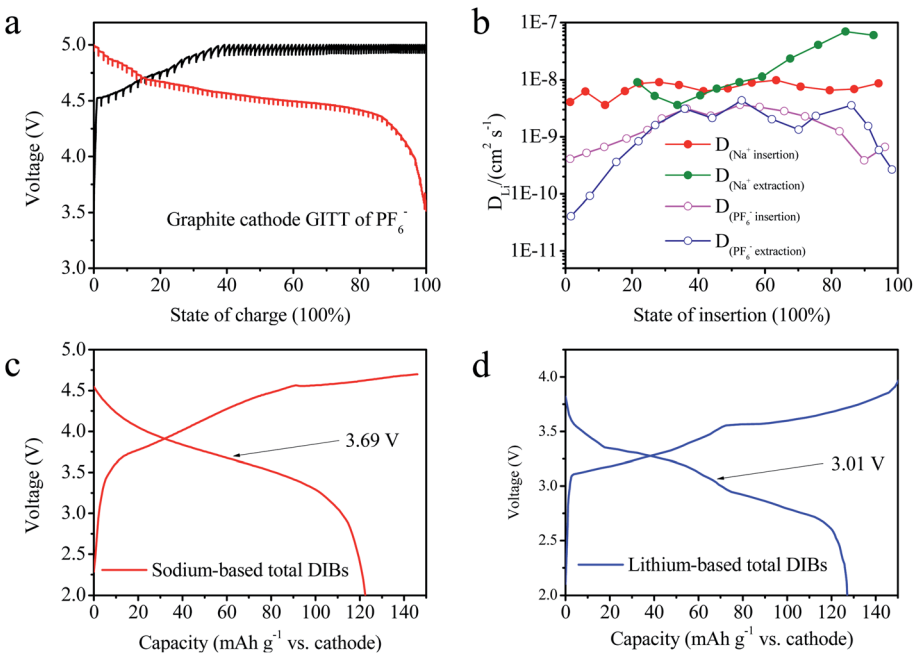

Fig. 6 (a) The GITT curves of the graphite cathode for the PF_6^- intercalation. (b) D of Na^+ and PF_6^- ions calculated from the GITT curves as a function of the voltage for the $Li_4Ti_5O_{12}$ anode and graphite cathode, respectively. Charge–discharge curves of sodium-based (c) and lithium-based (d) for total DIBs.

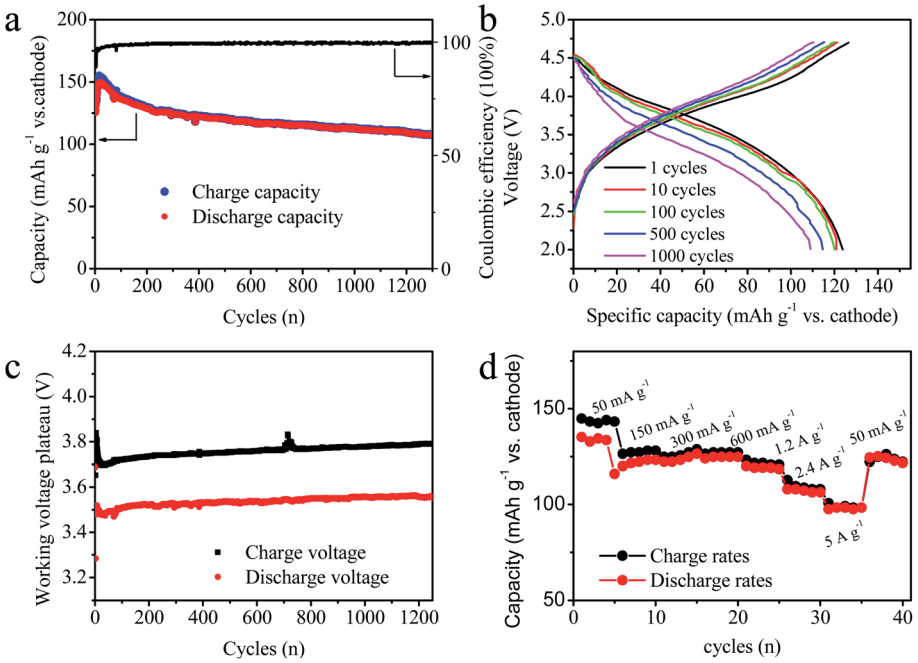

Fig. 7 (a) The cycling performance of full S-DIBs, (b) the charge–discharge curves at different cycles, and (c) the corresponding voltage plateaus at the middle capacity. (d) The rate performance at current density in the range of 50 mA h g^{-1} to 5000 mA g^{-1}.

slightly lower in poor-PF_6^- and rich-PF_6^-. Then, the value of D_{Na^+} is higher than that of $D_{PF_6^-}$ in graphite in the full batteries. Therefore, although the D_{Na^+} is lower than that of lithium ions (Fig. 3), the electrochemical performance of the sodium-based system is not limited when LTO and graphite are assembled into the system.

Fig. 6c demonstrates the charge–discharge curves of full DIBs (LTO|graphite), and the voltage is in the range of 2–4.6 V. With the excessive coating mass of the LTO anode, the full battery shows a charge capacity of 142 mA h g^{-1} and discharge capacity of 123 mA h g^{-1}. This capacity reflects a nominal capacity of the graphite cathode owing to the higher loading mass of the anode electrode. At the same time, the full battery also shows the voltage plateau of 3.68 V. In comparison, the Li-based full-batteries (Fig. 6d) exhibit a voltage platform of 3.02 V in the range of 4–2 V, which shows a relatively low energy density. Such a system has also been reported in the previous literature (Table S1†) but the performance of lithium titanate has reached that of industry materials in this article.

For long cycles in Fig. 7a, the full battery shows the capacity of 122 mA h g^{-1} in the initial stage, which steadily increased in the following cycles, which may be due to the gradual activation process of the anode that is initially caused by the difference in the specific capacities of the cathode and the anode. After 1200 cycles, the cell capacity remains stable at 106 mA h g^{-1}. By comparing the charge–discharge process, the (dis)charge capacity shows similar changing trends in cycling in Fig. 7b. However, the voltage plateau in the discharge curve still shows a certain drop, and the corresponding charging plateau increased slightly in Fig. 7c. For rate cycling, it can be seen that the capacity of the full battery remains relatively stable under different discharge current densities (50, 150, 300, 600, 1200, 2400, and 5000 mA h g^{-1}) in Fig. 7d. By testing the electrochemical performance, it proved that such a chemical system has great application potential, which cannot only overcome the shortage of sodium ion batteries in materials but also achieves higher energy density.

4 Conclusion

As an anode material with the structure of "zero strain", lithium titanate can maintain a relatively stable crystalline phase after intercalation by Na^+ instead of Li^+. Na^+-storage can decrease the average voltage (*vs.* Li/Li^+) of the anode to achieve the high working voltage in full DIBs (2–4.5 V). Comparing the diffusion properties of Na^+ and PF_6^- in the host materials, the transport rate of Na^+ in LTO is proved to meet the kinetic process between the anode and the cathode electrodes in assembled full batteries. Excellent electrochemical and stable storage performance reflects the application advantages of the sodium-guest energy storage system. These S-DIBs with the LTO anode can significantly enhance the energy density of the full batteries to trigger the industrial studies of Na^+-storage host materials.

Conflicts of interest

There are no conflicts to declare.

Acknowledgements

This work is financially supported by the Guangdong Innovation Research Team for High Education (2017KCXTD030), High-level Talents Project of Dongguan University of

Technology (KCYKYQD2017017), Research start-up funds of DGUT (GC300502-34).

References

1 J.-Y. Hwang, S.-T. Myung and Y.-K. Sun, *Chem. Soc. Rev.*, 2017, **46**, 3529.
2 Y. Niu, Y. Zhang and M. Xu, *J. Mater. Chem. A*, 2019, **7**, 15006.
3 L. Wang, J. Wang, D. H. L. Ng, S. Li, B. Zou, Y. Cui, X. Liu, S. A. El-Khodary, J. Qiu and J. Lian, *Chem. Commun.*, 2021, **57**, 9610–9613.
4 G. Subburam, K. Ramachandran, S. A. El-Khodary, B. Zou, J. Wang, L. Wang, J. Qiu, X. Liu, D. H. L. Ng and J. Lian, *Chem. Eng. J.*, 2021, **415**, 129012.
5 P. Meister, O. Fromm, S. Rothermel, J. Kasnatscheew, M. Winter and T. Placke, *Electrochim. Acta*, 2017, **228**, 18–27.
6 H.-J. Liao, Y.-M. Chen, Y.-T. Kao, J.-Y. An, Y.-H. Lai and D.-Y. Wang, *J. Phys. Chem. C*, 2017, **121**, 24463–24469.
7 G. Zhang, X. Ou, C. Cui, J. Ma, J. Yang and Y. Tang, *Adv. Funct. Mater.*, 2018, **29**, 1806722.
8 L. Fan, Q. Liu, S. Chen, Z. Xu and B. Lu, *Adv. Energy Mater.*, 2017, **7**, 1602778.
9 Z. Hu, Q. Liu, K. Zhang, L. Zhou, L. Li, M. Chen, Z. Tao, Y.-M. Kang, L. Mai, S.-L. Chou, J. Chen and S.-X. Dou, *ACS Appl. Mater. Interfaces*, 2018, **10**, 35978–35983.
10 T. Liu, Y. Zhang, Z. Jiang, X. Zeng, J. Ji, Z. Li, X. Gao, M. Sun, Z. Lin, M. Ling, J. Zheng and C. Liang, *Energy Environ. Sci.*, 2019, **12**, 1512.
11 T. Placke, A. Heckmann, R. Schmuch, P. Meister, K. Beltrop and M. Winter, *Joule*, 2018, **2**, 1–23.
12 L. Wu, D. Buchholz, D. Bresser, L. G. Chagas and S. Passerini, *J. Power Sources*, 2014, **251**, 379.
13 B. Zou, T. Wang, S. Li, R. Kang, G. Li, S. A. El-Khodary, D. H. L. Ng, X. Liu, J. Qiu, Y. Zhao, J. Lian and H. Li, *J. Energy Chem.*, 2021, **57**, 109–117.
14 Q. Guo, Q. Wang, G. Chen, Q. Shen and B. Li, *RSC Adv.*, 2016, **6**(111), 110032–110039.
15 Q. Guo, Q. Wang, G. Chen, H. Xu, J. Wu and B. Li, *ECS Trans.*, 2016, **72**(9), 11–23.
16 Y. Sun, L. Zhao, H. Pan, X. Lu, L. Gu, Y.-S. Hu, H. Li, M. Armand, Y. Ikuhara, L. Chen and X. Huang, *Nat. Commun.*, 2013, **4**, 1870.
17 M.-S. Kim, H.-K. Roh, J. Hui Jeong, G.-W. Lee, M. Nazarian-Samani, K. Y. Chung and K.-B. Kim, *J. Power Sources*, 2019, **409**, 48–57.
18 Q. Guo, Q. Wang, G. Chen, M. Shen and B. Li, *Mater. Trans.*, 2017, **58**(3), 383–389.
19 Y. Sun, S. Guo and H. Zhou, *Energy Environ. Sci.*, 2019, **12**, 825.
20 M. Zukalová, B. P. Lásková, M. Klementová and L. Kavan, *Electrochim. Acta*, 2017, **245**, 505–511.
21 G. Hasegawa, K. Kanamori, T. Kiyomura, H. Kurata, K. Nakanishi and T. Abe, *Adv. Energy Mater.*, 2015, **5**, 1400730.
22 K.-T. Kim, C.-Y. Yu, C. S. Yoon, S.-J. Kim, Y.-K. Sun and S.-T. Myung, *Nano Energy*, 2015, **12**, 725–734.
23 X. Wang, L. Qi and H. Wang, *ACS Appl. Mater. Interfaces*, 2019, **11**, 30453–30459.
24 Q. Ni, Y. Bai, Y. Li, L. Ling, L. Li, G. Chen, Z. Wang, H. Ren, F. Wu and C. Wu, *Small*, 2018, **14**, 1702864.
25 J. Tian, D. Cao, X. Zhou, J. Hu, M. Huang and C. Li, *ACS Nano*, 2018, **12**, 3424–3435.
26 X. H. Rui, N. Ding, J. Liu, C. Li and C. H. Chen, *Electrochim. Acta*, 2010, **55**, 2384–2390.
27 D. Ying, R. Ding, Y. Huang, W. Shi, Q. Xu, C. Tan, X. Sun, P. Gao and E. Liu, *J. Mater. Chem. A*, 2019, **7**, 18257–18266.
28 C. Li, T. Shi, H. H. Yoshitaked and H. Wang, *J. Mater. Chem. A*, 2016, **4**(43), 16982–16991.
29 W. Zhang, D.-H. Seo, T. Chen, L. Wu, M. Topsakal, Y. Zhu, D. Lu, G. Ceder and F. Wang, *Science*, 2020, **367**, 1030–1034.
30 M.-S. Kim, H.-K. Roh, J. H. Jeong, G.-W. Lee, M. Nazarian-Samani, K. Y. Chung and K.-B. Kim, *J. Power Sources*, 2019, **409**, 48–57.
31 B. Babu and M. M. Shaijumon, *J. Power Sources*, 2017, **353**, 85–94.
32 M. Michalska, M. Krajewski, D. Ziolkowska, B. Hamankiewicz, M. Andrzejczuk, L. Lipinska, K. P. Korona and A. Czerwinski, *Powder Technol.*, 2014, **266**, 372–377.
33 J. Jeong, M.-S. Kim, Y.-H. Kim, K. Roh and K.-B. Kim, *J. Power Sources*, 2016, **336**, 376–384.
34 D. Z. Liu, W. Hayes, M. Kurmoo, M. Dalton and C. Chen, *Physica C*, 1994, **235–240**, 1203–1204.
35 M. Kitta, K. Kuratani, M. Tabuchi, N. Takeichi, T. Akita, T. Kiyobayashi and M. Kohyama, *Electrochim. Acta*, 2014, **148**, 175–179.
36 L. Zhao, H.-L. Pan, Y.-S. Hu, H. Li and L.-Q. Chen, *Chin. Phys. B*, 2012, **21**, 028201.
37 S. Wang, W. Quan, Z. Zhu, Y. Yang, Q. Liu, Y. Ren, X. Zhang, R. Xu, Y. Hong, Z. Zhang, K. Amine, Z. Tang, J. Lu and J. Li, *Nat. Commun.*, 2017, **8**, 627.